Three-dimensional diffraction tomography using GPR

Clark Jorgensen[1] and Marvin Speece, Montana Tech, Alan Witten[2], Oak Ridge National Laboratory*

Summary

Ground Penetrating Radar (GPR) is a proven method of imaging the near subsurface. Most GPR interpretations rely on raw data records or records that have utilized standard seismic data processing packages. We have developed a method that will provide three-dimensional (3-D) images of the subsurface using geophysical diffraction tomography. The method described produces images of the subsurface for transmitting and receiving antennas on the surface at a fixed offset. The algorithm provides easily interpreted images and requires little specialized processing knowledge. These factors make it more useful than raw records and more usable than sophisticated migration techniques.

This method was tested using computer generated models and two field studies. The studies demonstrated the ability of diffraction tomography to image both conducting and nonconducting objects at known locations and the ease of use of the algorithm. Diffraction tomography for GPR data proved useful for generating accurate 3-D images of the subsurface.

Imaging Algorithm

By assuming the backscattered radiation from an object is weak, the radiation may be related to the object using the Helmholtz equation. Assuming the offset between the transmitting and receiving antennas is small, the 3-D Fourier transform of the object function may be related to the two-dimensional (2-D) transform of the scattered radiation field. By solving for this relationship for several different frequencies within the bandwidth of the transmitting antenna, an accurate representation of the object may be created. This imaging method is called 3-D diffraction tomography.

For the 2-D case the solution may be written as

$$U_s(k, z=0) \approx \frac{-k\, e^{-ip/4}}{4\sqrt{pg(k/2)}} \int dx\, dz\, \frac{O(x,z)}{\sqrt{|z|}}\, e^{-i[kx+2g(k/2)z]}$$

where $?(K)=v(k^2-K^2)$, $O(x,z)$ is the object function being solved, and $U_s(K,z=0)$ is the Fourier transformed scattered wavefield measured on the surface. The horizontal position x and the wavenumber K form a Fourier transform pair. The temporal wavenumber $k=?/v_o$ where ? is angular frequency and v_0 is the average background velocity. Details of this derivation may be found in Molyneaux and Witten (1993). For the 3-D case the solution is similar and may be written as

$$U_s(k, z=0) \approx \frac{ik}{8p} \int d\mathbf{r}\, dz\, \frac{O(\mathbf{r},z)}{|z|}\, e^{-i[k\bullet r+2g(k/2)z]}$$

where $?(\mathbf{K})=v(k^2-\mathbf{K}^2)$, $O(\mathbf{?},z)$ is the object function being solved, and $U_s(\mathbf{K},z=0)$ is the Fourier transformed scattered wavefield. The horizontal vector $\mathbf{?}=(x,y)$ forms a Fourier transform pair with $\mathbf{K}=(?_x,?_y)$. Mast and Johansson (1994) develop a similar 3-D algorithm for GPR and demonstrate its use.

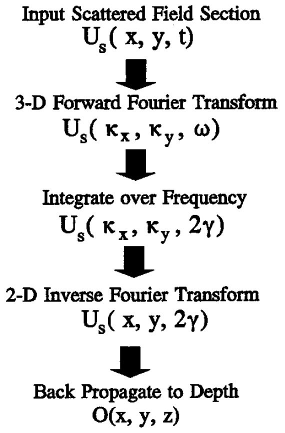

Fig. 1. Flow diagram for diffraction tomography algorithm.

This formulation for the object function is very similar to the reflectivity solution for Stolt's f-k migration (Stolt, 1978). If the values of ? were interpolated onto the Fourier grid, the object function could be obtained by taking the inverse transform of U_s. Unfortunately the integral for U_s given above is oscillatory and becomes increasingly inaccurate for large values of ? (Press, et.al., 1992, pp. 577-578). We therefore explicitly sum the values of the integral over z and

---

[1] presently Big Sky Geophysics

[2] presently School of Geology and Geophysics, University of Oklahoma

use a fast Fourier transform routine to evaluate the integral over **?**. Figure 1 shows the flow chart for this procedure.

Case Studies

Because of the similarity of this implementation of diffraction tomography with Stolt f-k migration, we examine a synthetic data set to compare the two methods. A cross section of the scattered field from two infinite cylinders is created using a finite difference seismic wave equation modeling program. We are able to utilize a seismic processing package because the scalar wave equation is the same for TE mode (electric dipoles oriented perpendicularly to profile direction) radar and seismic P-waves (compressional waves). The cross section is constructed using 64 stations for each source-receiver pair. The background velocity is 5000 ft/sec and each signal is sampled every 2 msec. Comparison of the Stolt migration and diffraction tomography (Figure 2) reveals the migration algorithm is more susceptible to dispersion. This is caused by interpolating data values for wavenumbers near the Nyquist value. Note that low velocity values correspond to positive reflectivity values. Both images were processed without any filtering or zero padding of the Fourier transform arrays.

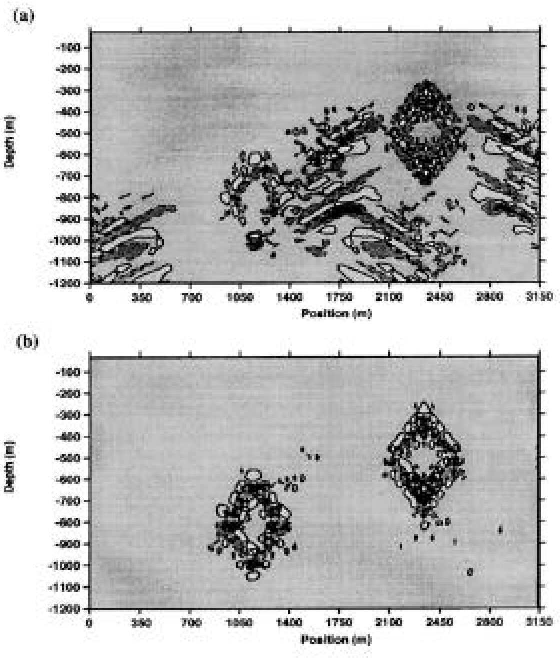

Fig. 2. Comparison of Stolt migration (a) and diffraction tomography (b) using finite difference modeling of two infinite cylinders centered at 800 and 500 feet depths with 200 feet radii. 64 source-receiver pairs with 20 feet offsets and 50 feet separations were used to generate the data. Low (high) velocities are represented by dark (light) colors.

In addition to the synthetic test, two field test sites were developed to test the algorithm. The little site consisted of a single metal 55 gallon drum centered at a depth of 1.8 meters in a 1.5 meter by 2.4 meter pit. The big site consisted of two metal 55 gallon drums and one plastic 55 gallon drum. One of the metal drums is standing and centered at a depth of 1.7 meters while the other metal drum is centered at 1.5 meters and the plastic drum is centered at 1.2 meters. The positioning of the drums is accurate to within 0.15 meter. The two pits were dug in sandy alluvial fill material with disseminated clays and black magnetite sands present. Inductive EM measurements of the sites before burial indicated a resistivity of approximately 100 Om in the shallow subsurface. Several profile lines using a magnetometer prior to burial indicated a relatively uniform magnetic response with all total field readings varying by less than 400 gammas. No clay layers of significance were observed in the small pit's walls but the large pit had a single clay lens of 0.3 to 0.5 meter thickness visible on all four walls. The clay lens was centered at a depth of approximately 1.1 meters.

A survey with a grid of 17 by 17 stations was conducted at the small test site with each station separated by 0.61 meter and an antenna separation of 0.61 meter. All profile lines were run from west to east using TE soundings. Figure 3 shows a schematic cross section of the barrel location in the pit and the raw data record recovered for the line located directly over the barrel. Only a modest bandpass filter and gain function have been applied to raw record. The diffraction curve is noticeable but not obvious. Figure 4 compares the results from processing only the single line of data (2-D processing) and processing the entire grid of data (3-D processing). Both figures were processed using the same gain and bandpass filtering functions used on the raw record. The 2 and 3-D processing techniques both exhibit smearing to the east. The 3-D processed profile has slightly better defined pit walls and a stronger amplitude response for the barrel. Otherwise the images are similar.

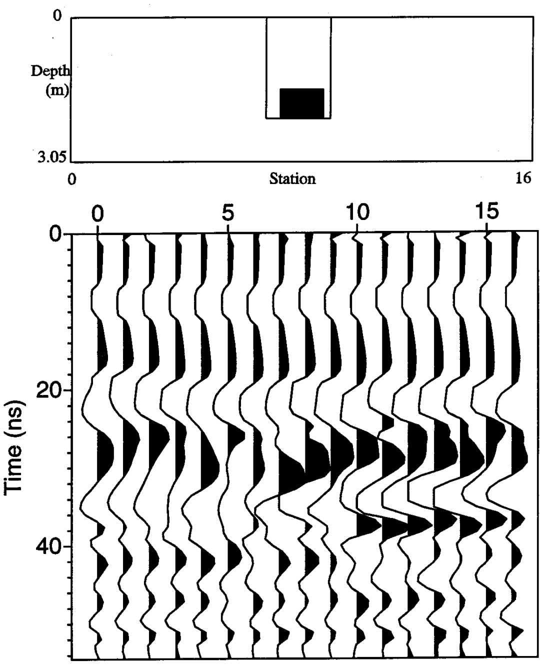

Fig. 3. Schematic drawing indicates barrel location in the pit. Raw wiggle trace plot of profile line over a metal drum buried on its side. The time window matches the depth cross section for an average velocity of 0.11 m/nsec.

The large test site was examined using a 41 by 41 grid of stations with a 0.30 meter separation between stations and a 0.61 meter offset between transmitter and receiver. The profile lines were run from west to east using TE antenna orientation. Figure 5 shows the raw record for the profile line located directly over the standing metal and horizontal plastic barrels. The same bandpass filter and gain were applied to Figure 5 as were applied to Figure 3. The diffraction from the metal barrel is apparent but it is difficult to detect any response from the plastic barrel. Figure 6 shows 2-D and 3-D processed data for the same profile line. Both the 2-D and 3-D processing methods used the same gain and filter functions used on the raw data. The low velocity anomaly at station 16 and depth of 1.5 meters corresponds with the top of the upright barrel. The high velocity anomaly at station 21 and depth of 1.2 meters corresponds to the center of the plastic barrel. The 2-D and 3-D methods both successfully indicate the barrel locations and the 3-D procedure increases the strength of the anomalies and indicates a multiple of the primary diffraction from the metal drum. There is no strong indication of image smearing at the large test site.

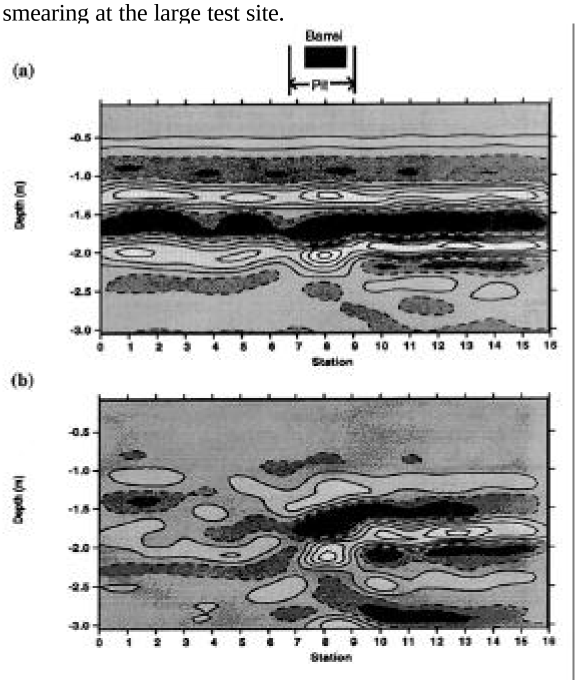

Fig. 4. Cross sections of 2-D (a) and 3-D (b) diffraction tomographic processing of raw data shown in Figure 3. The background velocity is 0.11 m/nsec. Low (high) velocities are indicated by dark (light) colors.

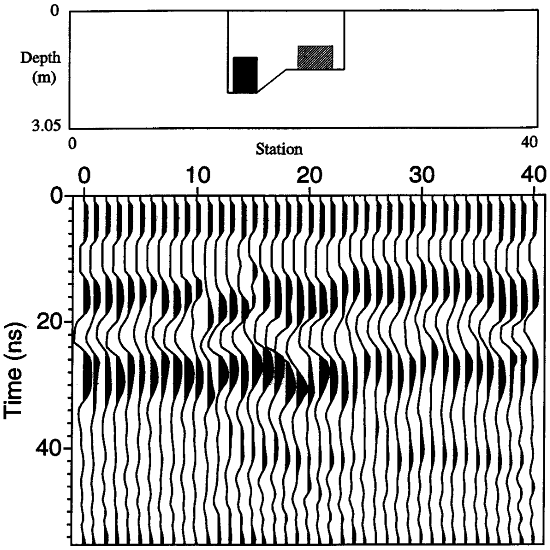

Fig. 5. Schematic drawing indicates barrel locations in the pit. Raw wiggle trace plot of profile line over a metal drum

(standing) and a plastic drum (on side). The time window matches the depth cross section for a velocity of 0.11 m/nsec.

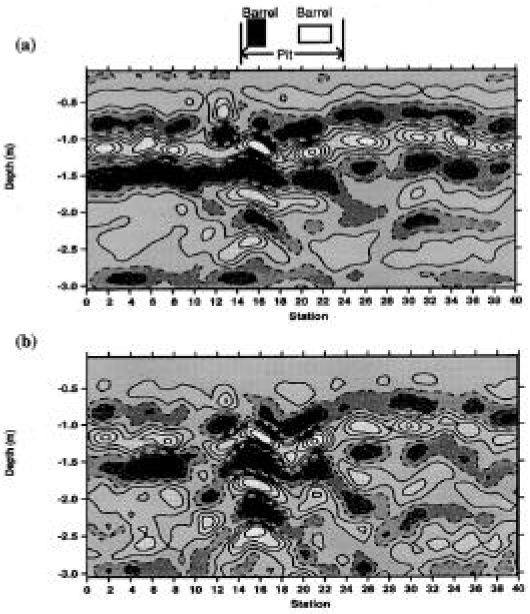

Fig. 6. Cross sections of 2-D (a) and 3-D (b) diffraction tomography processing of the raw data shown in Figure 5. The background velocity is 0.11 m/nsec. Low (high) velocities are indicated by dark (light) colors.

Discussion

The image responses correspond well with the barrels' locations. Low velocity anomalies are associated with the top of the metal barrels. Artificial high velocity anomalies occur inside the metal barrels that are associated with the reflection measurement geometry. The plastic barrel has a high velocity anomaly because the EM energy can travel at velocities near the speed of light in the interior of the barrel. All of the anomalies are located at their proper locations for the large test site but the low velocity anomaly for the barrel in the small pit is slightly deeper than it should be located. The top of the barrel is located at a depth of 1.5 meters but the anomaly is centered at a depth of 1.7 meters. The 3-D algorithm shows noticeable improvement at imaging the barrels. It is more effective at defining the pit walls for the large test pit than for the small test pit. This is surprising because the large pit contains more barrels and has a significant clay layer present, which create a more complex scattered field. The failure of the 3-D method to improve the imaging of the small pit walls may be due to spatial aliasing of the data because of the larger grid spacing or by wavefield dispersion caused by the magnetite.

Conclusions

Diffraction tomography is a useful method for imaging both conductive and nonconductive bodies using GPR. The method is easy to implement only requiring some simple bandpass filtering and gain function specifications by the user. Comparison with Stolt migration indicates it produces better images. Diffraction tomography provides a good balance between image enhancement without compromising ease of use. The use of 3-D processing generally improves images but is not effective in all cases.

Acknowledgements

This work was supported by a grant from the U.S. DOE under the Experimental Program to Stimulate Competitive Research (EPSCoR) and the Montana Organization for Research in Energy (MORE).

References

Mast, J.E. and Johansson, E.M., 1994, Three-dimensional ground penetrating radar imaging using multi-frequency diffraction tomography, SPIE, **2275**, paper no. 23.

Molyneux, J.E. and Witten, A., 1993, Diffraction tomographic imaging in a monostatic measurement geometry: IEEE Transactions on Geoscience and Remote Sensing, **31**, no. 2.

Press, W.H., Teukolsky, S.A., Vetterling, W.T., Flannery, B.P., 1992, Numerical Recipes in FORTRAN, Second Edition, Cambridge University Press, New York, NY, 963 p.

Stolt, R.H., 1978, Migration by Fourier transform, Geophysics, **43**, no. 1.